Interfacial waves generated by electrowetting-driven contact line motion

Jonghyun Ha,[1] Jaebum Park,[1] Yunhee Kim,[2] Bongsu Shin,[2] Jungmok Bae,[2] and Ho-Young Kim[1,a)]

[1]*Department of Mechanical and Aerospace Engineering, Seoul National University, Seoul 08826, South Korea*
[2]*Samsung Electronics Co., Ltd., Yongin, Gyeonggi-Do 17113, South Korea*

The contact angle of a liquid-fluid interface can be effectively modulated by the electrowetting-on-dielectric (EWOD) technology. Rapid movement of the contact line can be achieved by swift changes of voltage at the electrodes, which can give rise to interfacial waves under the strong influence of surface tension. Here we experimentally demonstrate EWOD-driven interfacial waves of overlapping liquids and compare their wavelength and decay length with the theoretical results obtained by a perturbation analysis. Our theory also allows us to predict the temporal evolution of the interfacial profiles in either rectangular or cylindrical containers, as driven by slipping contact lines. This work builds a theoretical framework to understand and predict the dynamics of capillary waves of a liquid-liquid interface driven by EWOD, which has practical implications on optofluidic devices used to guide light. *Published by AIP Publishing.* [http://dx.doi.org/10.1063/1.4963863]

I. INTRODUCTION

The boundary between two immiscible fluids is susceptible to waves when disturbed, as a result of exchange between the kinetic energy of the fluids and the potential energy either due to gravity or surface tension.[1] The waves with the wavelength much smaller than the capillary length, the length scale at which gravitational and surface tension effects are balanced, are referred to as the capillary waves. Here, we investigate the traveling capillary waves of liquid-liquid interfaces, which are excited at the contact line of the three phase of solid-liquid-liquid, by developing a novel flow excitation setup and employing a perturbation analysis. Unlike the waves of liquid-air interface where the air viscosity can be neglected frequently, the waves of the boundary between two viscous liquids are mathematically more involved and relatively harder to realize experimentally. Previous studies dealing with the waves of liquid-liquid interfaces have mainly employed analytical and numerical approaches,[2–4] to find temporal damping characteristics of the waves. On the other hand, our study is focused on the spatially developing profiles of the traveling waves of liquid-liquid interface, which have been rarely corroborated experimentally.

Our study of the interfacial waves of two immiscible liquids is motivated by a novel optofluidic device, a microliquid prism.[5,6] It steers a light beam by tilting a liquid-liquid interface acting as an optical refractive surface.[7] The current applications of the microprism array include telescopic optics,[8] laser radar,[9,10] solar lighting,[11] and three-dimensional displays.[12,13] In the microliquid prism, the liquid-liquid interface is actuated through EWOD (electrowetting-on-dielectric), which modulates the contact angle of interface on a dielectric surface by establishing an electrical potential difference between the dielectric-coated electrode and conducting liquid.[14] The electrowetting effect occurs as electrical charges are accumulated at the interface of electrolyte solution and electrode when the electrical field is applied, thereby lowering the solid-liquid surface energy and consequently the static contact angle.[15] The microliquid prism using EWOD is free of physical fatigue

---

a)Electronic address: hyk@snu.ac.kr

28, 102102-1

and noise owing to the absence of mechanically moving parts and consumes relatively small power. Detailed description of how to construct 3D displays using microliquid prisms can be found in Refs. 7, 16, and 17. The practical applications of prisms for 3D displays may require tilting of the refractive surface at over 3 kHz,[18] which may generate waves in the microliquid prism. Furthermore, high-frequency ac (alternating current) voltages are frequently adopted to stabilize the solid-liquid-liquid three-phase contact line,[19,20] which implies non-negligible fluctuations in the contact angle. This may also lead to ripples of interface.

With this practical implication in mind, the experimental setup employed in this work is unique compared with conventional apparatuses used to investigate interfacial waves in that the waves are provoked by slipping contact lines. This non-classical means of exciting surface waves can provide an effective tool to investigate the interfacial flow dynamics in small scale devices. To understand the interfacial waves under viscous effects theoretically, we perform a linear perturbation analysis based on the pioneering work of Lucassen-Reynders and Lucassen[21] in the Cartesian coordinates. We also extend the analysis to the cylindrical coordinates. Upon verifying the theory by measuring the wavelength and decay length as a function of frequency with experiment, we predict and corroborate the temporal evolution of liquid interface profile that is driven by the voltage change at the solid wall. In optofluidic prisms where the instantaneous shape of the refractive liquid interface determines optical images, the interface fluctuation affects the stability of optical images. Therefore, our study can help one to design the geometry and operation conditions of various optofluidic devices with minimal interfacial fluctuations.

II. EXPERIMENTAL

To observe the interfacial waves, we fabricated a liquid prism cell 5 mm in thickness. It measures 20 and 30 mm in width (d) and height ($3h$), respectively, as shown in Fig. 1. A plate in the left end is a glass wafer coated with ordered layers of molybdenum, silicon nitride, and parylene C. This is referred to as the EWOD plate where the modulations of contact angle and contact line position are carried out. The other end plate in the right is a mere glass imposing no electrical field. The side walls, through which optical observation is made, are the glass slides spin-coated with polytetrafluoroethylene having the contact angle of nearly 90° with the interface between two liquids. The cell was first filled with a 0.85 wt. % aqueous solution of polyacrylic acid (referred to as liquid 1) and then a mixture of 1% dodecane and 99% 1-chloronaphthalene (referred to as liquid 2). The total height of the liquids, $2h$, is 20 mm, and the top of the cell is exposed to air. The interface between these liquids is known to have a high refractive index of over 1.6 and robust electrowetting performance.[22] The density ρ and viscosity μ of the two liquids, and surface tension coefficient between them, γ, are listed in Table I. The square-wave ac voltage was applied to the EWOD plate using a voltage amplifier (AA Lab systems A-301 HS) connected to a function
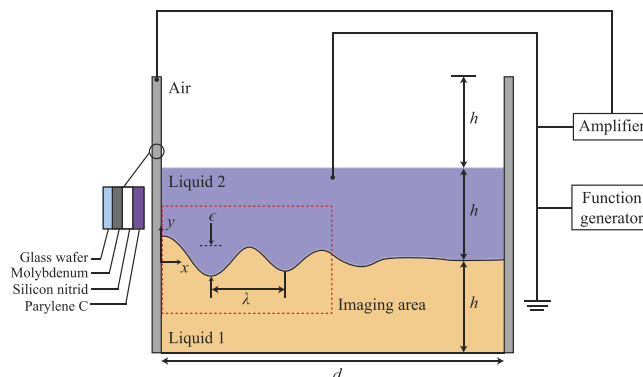

FIG. 1. Experimental setup to generate interfacial waves via EWOD. λ, ϵ, d, and h indicate the wavelength, amplitude, width of the prism cell (20 mm), and depth of liquids (10 mm), respectively.

TABLE I. Liquid properties.

	ρ (kg m^{-3})	μ (Pa s)	γ (mN m^{-1})
Liquid 1	1179	0.0027	7.64
Liquid 2	1000	0.0013	

generator (National Instruments NI9263) controlled by Labview (National Instruments). Liquid 2 was electrically grounded.

Figure 2 (Multimedia view) shows the images of the interfacial waves filmed by a high-speed video camera (Photron APX-RS) that recorded images at a rate of up to 1000 frames/s. As the voltage applied to the EWOD plate changes abruptly, the contact angle should be adjusted, accompanying the movement of contact line. The wave, generated by the slipping contact line, propagates toward the opposite side with wavelength and speed determined by the physical properties of the liquids and exciting ac frequency. The wavelength in the figure is 2 mm, which is significantly less than the crossover wavelength for capillary waves, $\lambda_c = 2\pi\sqrt{\gamma/(g\Delta\rho)} = 13$ mm, so that the capillary effects dominate over those of gravity. Here, $\Delta\rho = \rho_1 - \rho_2$ with subscripts 1 and 2 corresponding to liquids 1 and 2, respectively.

III. MATHEMATICAL MODELING

A. Waves in the Cartesian coordinates

The liquid-liquid interface profile can be described by a superposition of normal modes,

$$\eta(x,t) = \eta_0(x) + \text{Re}\left[\sum_{n=1}^{\infty} \eta_n(x,t)\right], \tag{1}$$

where η_0 and η_n represent the static meniscus and small perturbations, respectively. The static interfacial height at the EWOD wall is determined by the contact angle of the interface of two liquids with solid, which is a function of voltage. The static meniscus η_0 is given by $\eta_0 = a_0\exp(-x/l_c)$, where a_0 and l_c are arbitrary constant and capillary length ($l_c = \sqrt{\gamma/(g\Delta\rho)}$), respectively, a result of balance between capillary and gravitational effects.[23] Lucassen-Reynders and Lucassen[21] first considered the waves of interfaces of two overlapping viscous fluids in the Cartesian coordinates. We introduce the model in the following.
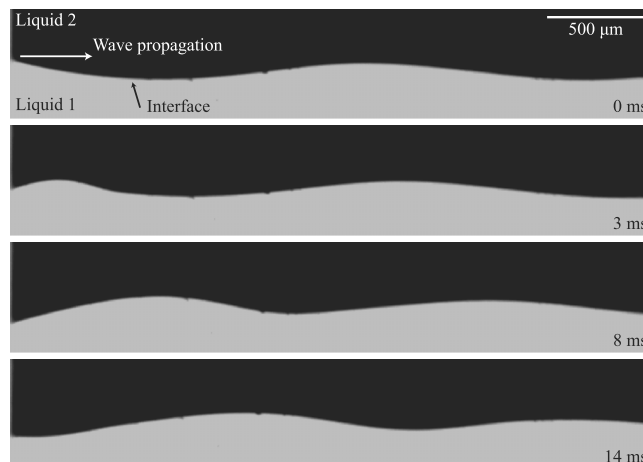

FIG. 2. Interfacial waves driven by EWOD under ac voltage of ±15 V with the frequency 50 Hz. The left side of the images coincides with the EWOD plate. (Multimedia view) [URL: http://dx.doi.org/10.1063/1.4963863.1]

Using a linear perturbation theory, the velocity and pressure of the fluids are expressed in the form of $\exp[i(\zeta x - \omega t)]$, where ω is the angular frequency and $\mathrm{Re}[\zeta] = k$ is the wavenumber: $k = 2\pi/\lambda$ with λ being the wavelength. $\mathrm{Im}[\zeta] = \alpha$ is the damping coefficient, which results in the attenuation of the velocity and pressure difference. Lamb[24] expressed the flow field of viscous liquids as

$$u_j = \frac{\partial \phi_j}{\partial x} - \frac{\partial \psi_j}{\partial y}, \tag{2}$$

$$v_j = \frac{\partial \phi_j}{\partial y} + \frac{\partial \psi_j}{\partial x}, \tag{3}$$

where u and v correspond to the velocity in the x and y directions, ϕ is the velocity potential of irrotational flow, and ψ is the stream function of rotational flow. The subscripts $j = 1$ and 2 correspond to liquids 1 ($y < 0$) and 2 ($y > 0$), respectively. We assume that the wave system has an infinite depth for $h \gg \lambda$. The irrotational flow satisfies the continuity equation $\nabla^2 \phi_j = 0$, whose boundary conditions are such that $\phi_1 \mid_{y \to -\infty} = 0$ and $\phi_2 \mid_{y \to \infty} = 0$. Then the solutions can be expressed as $\phi_1 = A_1 e^{\zeta y} \exp[i(\zeta x - \omega t)]$ and $\phi_2 = A_2 e^{-\zeta y} \exp[i(\zeta x - \omega t)]$, where A_1 and A_2 are the coefficients. The pressure can then be expressed by the linearized unsteady Bernoulli equation,

$$p_1 = -\rho_1 \frac{\partial \phi}{\partial t} = i\rho_1 \omega A_1 e^{\zeta y} \exp[i(\zeta x - \omega t)], \tag{4}$$

$$p_2 = -\rho_2 \frac{\partial \phi}{\partial t} = i\rho_2 \omega A_2 e^{-\zeta y} \exp[i(\zeta x - \omega t)]. \tag{5}$$

By taking curl of the Navier-Stokes equation and using vector identity, one can show that $\partial \psi_j/\partial t = \nu_j \nabla^2 \psi_j$, where ν is the kinematic viscosity. The solutions of the rotational flow can be written as $\psi_1 = B_1 e^{m_1 y} \exp[i(\zeta x - \omega t)]$ and $\psi_2 = B_2 e^{-m_2 y} \exp[i(\zeta x - \omega t)]$, where $m_j = \sqrt{\zeta^2 - i\omega/\nu_j}$, and B_1 and B_2 are the coefficients. Now the velocities of liquids 1 and 2 are given by

$$u_1 = (i\zeta A_1 e^{\zeta y} - m_1 B_1 e^{m_1 y}) \exp[i(\zeta x - \omega t)], \tag{6}$$

$$u_2 = (i\zeta A_2 e^{-\zeta y} + m_2 B_2 e^{-m_2 y}) \exp[i(\zeta x - \omega t)], \tag{7}$$

$$v_1 = (\zeta A_1 e^{\zeta y} + i\zeta B_1 e^{m_1 y}) \exp[i(\zeta x - \omega t)], \tag{8}$$

$$v_2 = (-\zeta A_2 e^{-\zeta y} + i\zeta B_2 e^{-m_2 y}) \exp[i(\zeta x - \omega t)]. \tag{9}$$

For the overlapping liquids, the following boundary conditions can be established at the liquid interface, $y = 0$. The kinematic boundary conditions are such that velocities of each liquid are continuous in the tangential and normal directions: $u_1 = u_2$ and $v_1 = v_2 = \partial \eta/\partial t$. The dynamic boundary conditions consist of the conditions for tangential and normal stresses. The tangential stresses are continuous, so that $\mu_1(\partial v_1/\partial x + \partial u_1/\partial y) = \mu_2(\partial v_2/\partial x + \partial u_2/\partial y)$. The difference between the normal stresses (pressure) is balanced by the surface tension multiplied by the curvature, so that $p_2 - p_1 = \gamma \partial^2 \eta/\partial x^2$. Substituting the velocity and pressure functions for liquids 1 and 2 into the boundary conditions yields four linear homogeneous equations. For nontrivial solutions of A_1, A_2, B_1, and B_2, the determinant of the matrix of coefficients should be zero,

$$\mathrm{Det} \begin{bmatrix} i\zeta & -i\zeta & -m_1 & -m_2 \\ 1 & 1 & i & -i \\ i2\mu_1\zeta^2 & i2\mu_2\zeta^2 & -\mu_1(m_1^2 + \zeta^2) & \mu_2(m_2^2 + \zeta^2) \\ i\left(\frac{\gamma\zeta^3}{\omega} - \rho_1\omega\right) & i\rho_2\omega & -\frac{\gamma\zeta^3}{\omega} & 0 \end{bmatrix} = 0. \tag{10}$$

The value of η satisfying Eq. (10) must meet the physical requirements that the wavenumber k and damping coefficient α are positive.

To nondimensionalize Eq. (10), we take the characteristic length by using crossover wavelength $\lambda_c = 2\pi\sqrt{\gamma/(g\Delta\rho)}$ and the characteristic frequency $\omega_c = \sqrt{\gamma/(\rho_1 + \rho_2)(2\pi/\lambda_c)^3}$. The characteristic density and viscosity are $\rho_c = \rho_1 + \rho_2$ and $\mu_c = \mu_1 + \mu_2$, respectively. The values listed in Table I gives $\omega_c = 20$ Hz. The dimensionless form of Eq. (10) is then given by

$$\mathrm{Det}\begin{bmatrix} i\hat{\zeta} & -i\hat{\zeta} & -\hat{m}_1 & -\hat{m}_2 \\ 1 & 1 & i & -i \\ i2q_1\hat{\zeta}^2 & i2q_2\hat{\zeta}^2 & -q_1(\hat{m}_1^2 + \hat{\zeta}^2) & q_2(\hat{m}_2^2 + \hat{\zeta}^2) \\ i\left(\dfrac{\hat{\zeta}^3}{\hat{\omega}}Ca^{-1} - h_1\hat{\omega}Re\right) & ih_2\hat{\omega}Re & -\dfrac{\hat{\zeta}^3}{\hat{\omega}}Ca^{-1} & 0 \end{bmatrix} = 0, \tag{11}$$

where $\hat{\zeta} = \zeta/\lambda_c$, $\hat{\omega} = \omega/\omega_c$, $q_j = \mu_j/\mu_c$, $h_j = \rho_j/\rho_c$, $\hat{m}_j^2 = \hat{\zeta}^2 - ih_j/q_j\hat{\omega}Re$, $Ca = \mu_c\lambda_c\omega_c/\gamma$, and $Re = \rho_c\lambda_c^2\omega_c/\mu_c$. Capillary number Ca and Reynolds number Re are the dimensionless surface tension coefficient and density in this wave system, respectively.

Before turning to the cylindrical coordinates, it is noted that we neglect the viscous resistances in the wedge region near the moving contact line and the boundary layer near the flow cell walls in our modeling. The former is ignored in view of small wave amplitude relative to the wavelength, which characterizes the wedge size as compared with the overall flow dimension.[25] The thickness of boundary layer near the wall, δ, can be estimated as $\delta \sim \sqrt{\nu/f}$, where ν can be considered as the average kinematic viscosity of the liquids and f is the excitation frequency. The value of δ ranges from 94 to 423 μm as the frequency varies from 200 to 10 Hz in our experimental conditions, thus much smaller than the wavelength (varying from 0.7 to 5.5 mm) as well as the thickness (5 mm) of the flow cell.

B. Waves in the cylindrical coordinates

For interfacial waves of overlapping liquids in a cylindrical container, we newly modify the foregoing theory[21] using the cylindrical coordinates (r, z). For a system with rotational symmetry, we write the velocity as[26]

$$u_r = \frac{\partial\phi}{\partial r} - \frac{1}{r}\frac{\partial\psi}{\partial z}, \tag{12}$$

$$u_z = \frac{\partial\phi}{\partial z} + \frac{1}{r}\frac{\partial\psi}{\partial r}. \tag{13}$$

As velocity potentials satisfying the continuity equation $\nabla^2\phi_j = 0$, we write $\phi_1 = A_1J_0(\zeta r)e^z e^{i\omega t}$ and $\phi_2 = A_2J_0(\zeta r)e^{-z}e^{i\omega t}$, where $J_0(\zeta r)$ is the zeroth order Bessel function of the first kind. The pressure function can then be derived by the unsteady Bernoulli equation, similar to the process described for the Cartesian system. The solutions of the rotational flow ψ that satisfy the modified Navier-Stokes equation $\rho\partial\psi_j/\partial t = \mu(\nabla^2\psi_j - 2/r\partial\psi_j/\partial r)$ can be written as $\psi_1 = B_1rJ_1(\zeta r)e^{s_1 z}e^{i\omega t}$ and $\psi_2 = B_2rJ_1(\zeta r)e^{-s_2 z}e^{i\omega t}$, where $s_j = \sqrt{\zeta^2 + i\omega/\nu_j}$ and $J_1(\zeta r)$ is the first-order Bessel function of the first kind. The velocity and pressure can then be expressed as

$$u_{r1} = \left(-\zeta A_1 e^{\zeta z} - s_1 B_1 e^{s_1 z}\right) J_1(\zeta r)e^{i\omega t}, \tag{14}$$

$$u_{r2} = \left(-\zeta A_2 e^{-\zeta z} + s_2 B_2 e^{-s_2 z}\right) J_1(\zeta r)e^{i\omega t}, \tag{15}$$

$$u_{z1} = \left(\zeta A_1 e^{\zeta z} + \zeta B_1 e^{s_1 z}\right) J_0(\zeta r)e^{i\omega t}, \tag{16}$$

$$u_{z2} = \left(-\zeta A_2 e^{-\zeta z} + \zeta B_2 e^{s_2 z}\right) J_0(\zeta r)e^{i\omega t}, \tag{17}$$

$$p_1 = -i\rho_1\omega A_1 J_0(\zeta r)e^{\zeta z}e^{i\omega t}, \tag{18}$$

$$p_2 = -i\rho_1\omega A_2 J_0(\zeta r)e^{-\zeta z}e^{i\omega t}. \tag{19}$$

Imposing the same boundary conditions as in the Cartesian coordinates, we get the following dimensionless equation:

$$\text{Det}\begin{bmatrix} \hat{\zeta} & -\hat{\zeta} & \hat{s}_1 & \hat{s}_2 \\ 1 & 1 & 1 & -1 \\ 2q_1\hat{\zeta}^2 & 2q_2\hat{\zeta}^2 & q_1(\hat{s}_1^2 + \hat{\zeta}^2) & -q_2(\hat{s}_2^2 + \hat{\zeta}^2) \\ i\left(\dfrac{\hat{\zeta}^3}{\hat{\omega}}Ca^{-1} - h_1\hat{\omega}Re\right) & ih_2\hat{\omega}Re & i\dfrac{\hat{\zeta}^3}{\hat{\omega}}Ca^{-1} & 0 \end{bmatrix} = 0, \tag{20}$$

where $\hat{s}_j^2 = \hat{\zeta}^2 + ih_j/q_j\hat{\omega}Re$. For the waves that propagate to the center of the cylinder, $\text{Re}[\zeta]$ and $\text{Im}[\zeta]$ are positive and negative, respectively.

IV. RESULTS AND DISCUSSION

A. Waves in the rectangular container

Figure 3(a) shows an instantaneous profile of wave generated in the setup of Fig. 1 driven by a square-wave ac of ± 20 V at 50 Hz when the contact line at $x = 0$ starts to rise. The wavelength λ is defined as the distance from the first two crests. To find the damping coefficient α, we consider the envelope of the excited waves as shown in Fig. 3(b). We then choose four positions along the x-direction at intervals of approximately 1 mm and measure the average value of the exponential decrease of the amplitude at each point: $\alpha = \text{Average}[\ln(C_m/C_n)/(x_n - x_m)]$ for $m > n$. Figure 4 shows that both the wavelength and the decay length decrease with an increase of frequency while displaying good agreement between experiment and theory. The inset of Fig. 4 compares the characteristics of liquid-air and liquid-liquid interfacial waves, to reveal substantial differences of the wavelength and decay length. The wavelength of the liquid-liquid interface is shorter than the liquid-air interface, e.g., 1.2 versus 3.5 mm for 100 Hz. The decay length of the liquid-liquid interfacial wave is much shorter than that for the liquid-air interfacial wave, e.g., 2.4 versus 167.2 mm for 100 Hz. These results clearly demonstrate the effects of the second fluid phase on the wave characteristics.

Linear perturbation analysis that predicts the wavelength and decay length also allows us to approximate the wave profile as a function of time. We note that the oscillation of the interface location at the EWOD wall cannot be prescribed *a priori* because the temporal evolution of the contact angle due to voltage change is a result of complicated electrochemical interaction of the electrolyte solution and solid surface material. Thus, we obtain the height profile experimentally as shown in Fig. 5(a). The contact line returns to the original position in 0.1 s as driven by square-wave ac of 10 Hz frequency, but its position hardly changes like a square wave with time. We obtain the Fourier coefficients a_n and b_n up to the eighth mode by curve fitting, and then the contact line
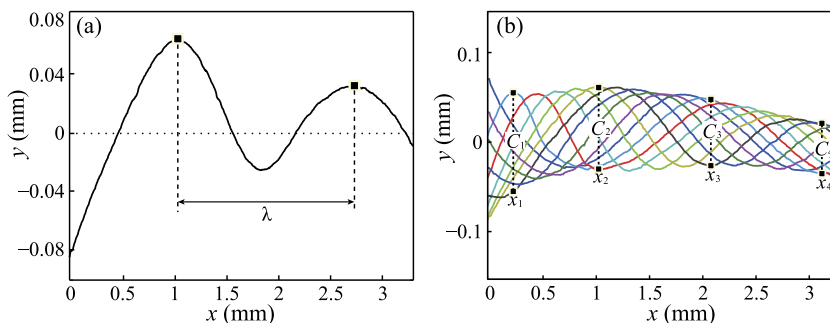

FIG. 3. Experimentally measured interfacial wave profiles near the EWOD plate driven at 50 Hz with ± 20 V. (a) The distance between two filled squares indicates wavelength, $\lambda = 1.7$ mm. (b) Measurement of the damping coefficient α for the wave imaged at different instants. α is measured to be 0.23 mm^{-1}.
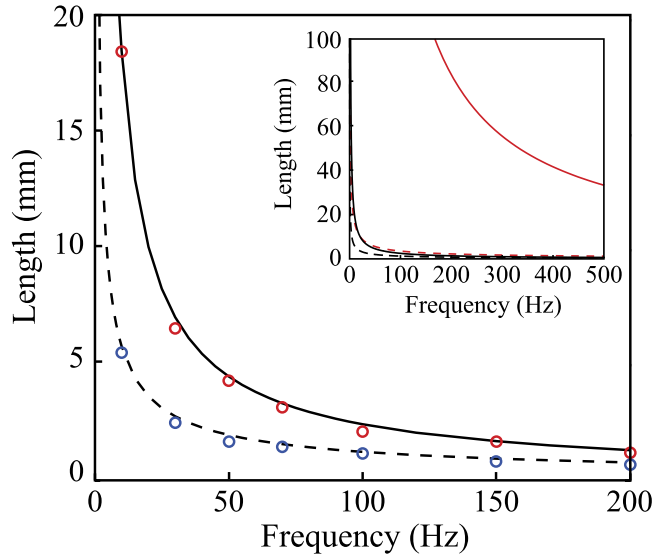
FIG. 4. Comparison between theoretically predicted wavelength and decay length obtained by solving Eq. (10) and experimental measurements. Dashed and solid lines are theoretical wavelength λ and decay length $L = 1/\alpha$, respectively. Blue and red circles are experimental wavelength and decay length, respectively. Error bars are not shown because they are smaller than the circles. Inset, comparison between the characteristics of liquid-liquid interface (black lines) and liquid-air interface (red lines). The dashed lines correspond to the wavelength, and the solid lines to the decay length. In the computation for liquid-air interface, the properties of liquid 2 have been replaced by those of air, i.e., $\rho_2 = 1.2$ kg/m^3, $\mu_2 = 0.01$ mPa·s, and $\gamma = 70$ mN m^{-1}.

location is given by

$$\text{Re}[\eta(0,t)] = a_0 + \sum_{n=1}^{N} \left[a_n \cos(\omega_n t) + b_n \sin(\omega_n t) \right], \tag{21}$$

where $N = 8$ and $\omega_n = n\omega_1$ with ω_1 being 2π times the excitation frequency.

Equation (1) is now rewritten to construct the interface profile as

$$\text{Re}[\eta(x,t)] = a_0 e^{-x/l_c} + \sum_{n=1}^{N} \left\{ [a_n \cos(k_n x - \omega_n t) - b_n \sin(k_n x - \omega_n t)] e^{-\alpha_n x} \right\}, \tag{22}$$
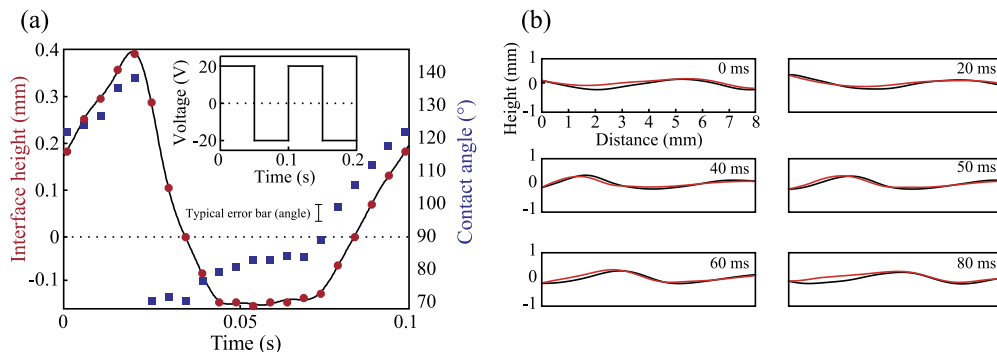

FIG. 5. (a) Temporal evolution of the contact line position (red circles) and the contact angle of liquid 2 (blue squares) on the EWOD wall as excited at the frequency of 10 Hz. The solid line is a curve fitting for the experimentally measured data (circles). Inset, voltage profile with time. (b) Time sequence of the interfacial waves driven by the boundary oscillation of Fig. 5(a). The black and red lines correspond to theory and experiment, respectively. (Multimedia view) [URL: http://dx.doi.org/10.1063/1.4963863.2]
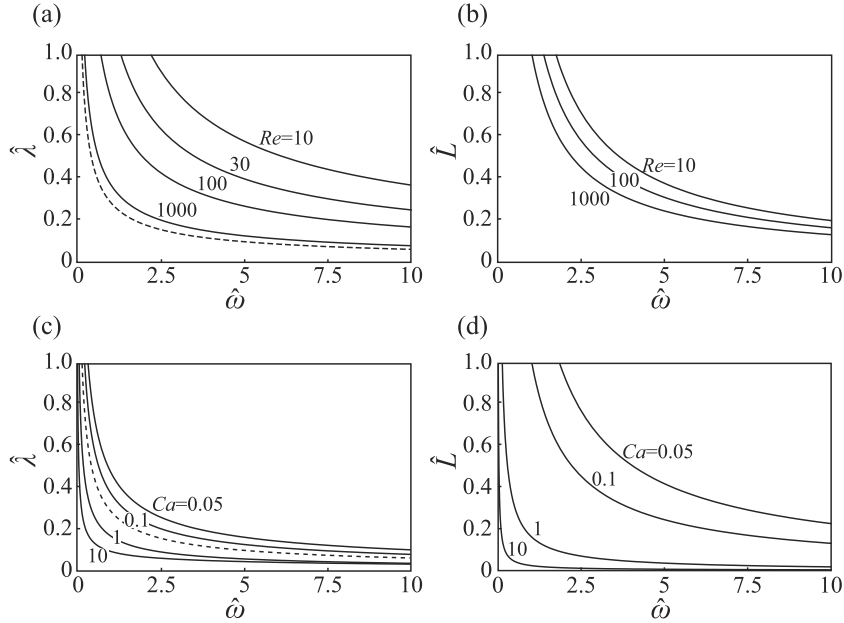
FIG. 6. (a) Dimensionless wavelength, $\hat{\lambda}$, and (b) decay length, $\hat{L}$, versus $\hat{\omega}$ for varying Re with Ca fixed at 0.1. (c) $\hat{\lambda}$ and (d) $\hat{L}$ for varying Ca with Re fixed at 1000. In all the cases, $h_j = q_j = 0.5$. Dashed lines in (a) and (c) correspond to the inviscid dispersion relation, $\hat{\lambda} = 2\pi(\rho_c \lambda_c^3 \omega_c^2 \hat{\omega}^2 / \gamma)^{-1/3}$.

where a_0, a_n, and b_n are identical to those in Eq. (21). The real and imaginary parts of ζ, k_n, and α_n, respectively, are obtained by solving Eq. (11) for the corresponding ω_n. In Fig. 5(b) (Multimedia view), we plot the theoretical wave profiles corresponding to the contact line oscillation as given by Fig. 5(a) and compare them with the experimental observations. We see favorable agreement between theory and experiment. Although the effects of the side walls in the z-direction and the change of liquid properties (μ and σ) due to lighting used for high-speed imaging appear to cause finite discrepancy between our two-dimensional theory and experiment, our model still captures the essential features (e.g., wavelength, amplitude, propagation speed, and decay length) of the interfacial waves.

Using theory, we now conduct a parametric analysis to see the effects of liquid properties, i.e., density, viscosity, and surface tension, on the wavelength and decay length of the interfacial waves. As seen in Eq. (11), $\hat{\zeta}$ is a function of q_j, h_j, Re, and Ca, which depend on the liquid properties, as well as $\hat{\omega}$. Our calculations revealed that h_j and q_j have far less pronounced effects on the wave characteristics than those of Re and Ca. In Fig. 6, therefore, we plot dimensionless wavelength $\hat{\lambda} = \lambda/\lambda_c$ and decay length $\hat{L} = L/\lambda_c$ versus dimensionless frequency $\hat{\omega} = \omega/\omega_c$ while varying Re and Ca. An increase in Re shortens both the wavelength and decay length, Figs. 6(a) and 6(b). An increase in Ca decreases the wavelength at a given frequency, as shown in Fig. 6(c), and the decay length behaves in a similar manner, Fig. 6(d). We also find that the effects of varying Re are severer on the wavelength than on decay length, while varying Ca exerts more significant influences on decay length than on the wavelength.

Before turning to the waves in cylindrical containers, we illustrate how the wave profile affects the path of light that passes through the liquid-liquid interface in the Appendix. Using a basic theory of optics,[27,28] we can predict the scattering characteristics of light depending on the shape of the refractive surface. This calculation is one of the most important steps in designing a liquid prism to achieve sharp optical images. We emphasize that the calculation of the traveling wave profile as carried out in this work can play a pivotal role in the prediction of optical images constructed by a liquid prism driven by EWOD.

B. Waves in cylindrical containers

Despite the similar forms of dispersion relation in Eqs. (11) and (20), the interface profiles in the cylindrical coordinates are fairly different from those in the Cartesian coordinates. Interface profiles in the cylindrical coordinates can be expressed as $\mathrm{Re}[\eta(r,t)] = \mathrm{Re}[-i\zeta\omega^{-1}(A_1 + B_1)J_0(\zeta r)e^{i\omega t}]$. The amplitude at the wall, $a_b = \mathrm{Re}[\eta(R,t)_{\max}]$, is determined by such factors as the characteristics of dielectric layer, frequency, and liquid properties. We nondimensionalize surface profiles with a_b: $\mathrm{Re}[\hat{\eta}(\hat{r},t)] = \hat{\epsilon}(\hat{r})\cos(\omega t - \theta(\hat{r}))$, where $\hat{r}$ is the dimensionless radius $\hat{r} = r/R$ with R being the radius of the cylindrical container. $\hat{\epsilon}(\hat{r})$ and $\theta(\hat{r})$ are the dimensionless amplitude and phase functions, respectively, and written as

$$\hat{\epsilon}(\hat{r}) = \sqrt{\frac{\mathrm{Im}[J_0(\hat{\zeta}\hat{r}\hat{R})]^2 + \mathrm{Re}[J_0(\hat{\zeta}\hat{r}\hat{R})]^2}{\mathrm{Im}[J_0(\hat{\zeta}\hat{R})]^2 + \mathrm{Re}[J_0(\hat{\zeta}\hat{R})]^2}}, \tag{23}$$

$$\theta(\hat{r}) = \tan^{-1}\left\{\frac{\mathrm{Re}[J_0(\hat{\zeta}\hat{r}\hat{R})]}{\mathrm{Im}[J_0(\hat{\zeta}\hat{r}\hat{R})]}\right\}, \tag{24}$$

where $\hat{R} = R/\lambda_c$. The top row of Fig. 7 (Multimedia view) displays the interfacial profiles, $\mathrm{Re}[\hat{\eta}(\hat{r},t)]$, in different sizes of containers under the excitation frequency of 50 Hz. The bottom row plots the dimensionless amplitude $\hat{\epsilon}(\hat{r})$ for different frequencies.

The wave amplitude at the center, $\hat{\epsilon}(0)$, is a result of the superposition of interfacial waves propagating from the wall to the center. While the amplitude decays exponentially in the Cartesian coordinates due to viscous effects, it may oscillate (because of inherent features of the Bessel function with complex number ζ) with $\hat{r}$ near the center as clearly shown in the bottom row of Fig. 7(a). Also, we see that $\hat{\epsilon}(\hat{r})$ converges to $e^{\hat{\alpha}\hat{R}(\hat{r}-1)}$, a similar form to that for the Cartesian coordinates, with increases in both $\hat{\omega}$ and $\hat{R}$.

These salient features of the waves in the cylindrical coordinates lead us to investigate the effects of frequency and cylinder radius on the wave amplitude at the center, $\hat{\epsilon}(0)$,

$$\hat{\epsilon}(0) = \frac{1}{\sqrt{\mathrm{Im}[J_0(\hat{\zeta}\hat{R})]^2 + \mathrm{Re}[J_0(\hat{\zeta}\hat{R})]^2}}. \tag{25}$$

Because the Bessel function J_0 oscillates with complex arguments, $\hat{\epsilon}(0)$ fluctuates severely when the magnitude of $\hat{\zeta}\hat{R}$ is small. Figure 8(a) plots $\hat{\epsilon}(0)$ versus $\hat{\omega}$ for different values of $\hat{R}$. Whenever the
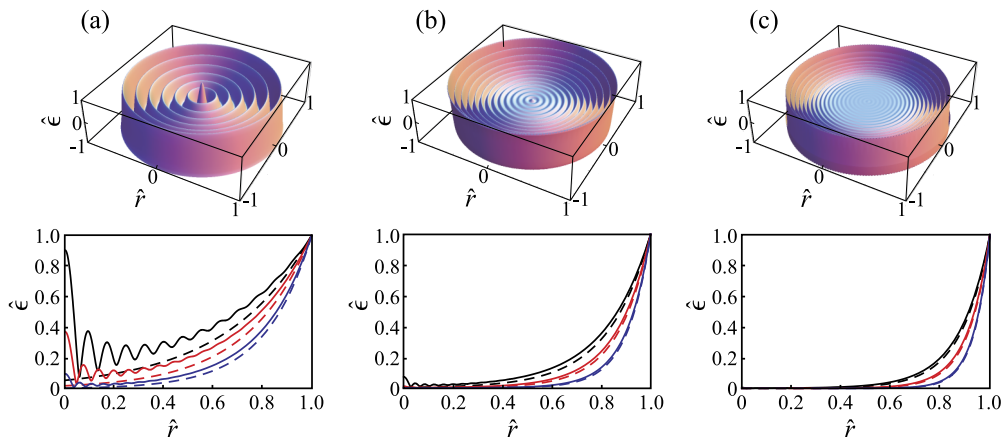

FIG. 7. Interfacial profiles of the overlapping liquids at $t = 0$, when the displacement at the center is maximized, in cylindrical containers of $\hat{R} = 1$ (a), 2 (b), and 3 (c). The top row displays tilted-view snapshots of waves for excitation of 50 Hz. Black, red, and blue lines in the bottom row, $\hat{\epsilon}$ versus $\hat{r}$, correspond to the frequency of 50, 70, and 100 Hz (or $\hat{\omega} = 2.5,\ 3.5,$ and 5), respectively. Solid and dashed lines are the theoretical results for the cylindrical and Cartesian coordinates, respectively. (Multimedia view) [URL: http://dx.doi.org/10.1063/1.4963863.3]
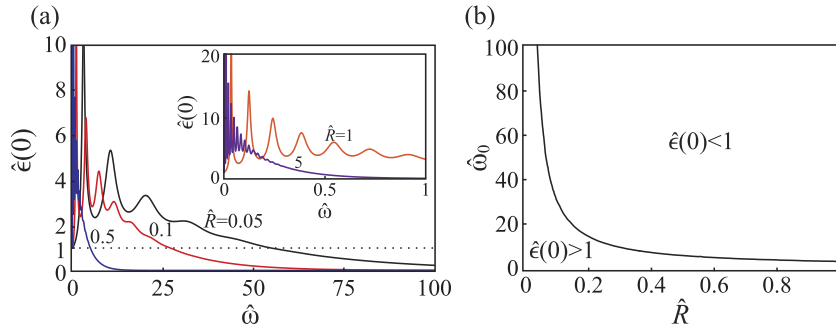
FIG. 8. (a) Wave amplitude at the center versus frequency for varying $\hat{R}$. (b) The critical frequency $\hat{\omega}_0$ at which $\hat{\epsilon}(0) = 1$ versus $\hat{R}$. It is recommended that the device is run at a frequency higher than the critical frequency to ensure predictable wave dynamics. In the computations, $Ca = 0.1$, $Re = 1000$, and $h_j = q_j = 0.5$.

denominator of $\hat{\epsilon}(0)$ approaches zero with varying $\hat{\omega}$ that determines $\hat{\zeta}$ by Eq. (20), the dimensionless amplitude at the center becomes very large as indicated by repeated peaks in Fig. 8(a), which are greater than the oscillation amplitude at the wall. At a constant $\hat{R}$, $\hat{\epsilon}(0)$ is always higher than 1, or the amplitude is higher at the center than at the wall, for very low frequency, but it falls below 1 as $\hat{\omega}$ increases. We plot the dimensionless frequency $\hat{\omega}_0$ at which $\hat{\epsilon}(0) = 1$ as a function of $\hat{R}$ in Fig. 8(b). The range of $\hat{\omega}$ where $\hat{\epsilon}(0) > 1$ decreases with the increase of $\hat{R}$. Our theory suggests an important guide for the design of cylindrical liquid prisms or similar shapes. The operation frequency and prism size should be sufficiently large to avoid large fluctuations of wave amplitude near center, which can be caused by a slight change of the frequency and container dimension. That is, our theory provides a frequency range which can ensure stably attenuating waves in a cylindrical container of the given radius.

V. CONCLUSIONS

We experimentally visualized and theoretically analyzed the interfacial waves in the liquid prism operated by EWOD actuation. We obtained the wavelength and decay length of the interfacial waves as a function of frequency while considering viscous effects. Furthermore, we investigated the effects of liquid properties on wave characteristics by parametric analysis. The wavelength was found to decrease with an increase in density, and the decay length decreases with an increase in viscosity. Both the wavelength and the decay length increase with an increase in interfacial tension, a ramification of strong potential energy. The theory, which was experimentally verified with an experimental setup adopting a long rectangular flow cell, was then extended to a cylindrical geometry bearing a more intimate implication on the liquid prism design. The waves, expressed with the Bessel functions, were shown to propagate toward the center and sometimes exhibit non-monotonous decay of amplitude. Our theory reveals that the operation frequency and cell size should be sufficiently large to ensure monotonically decaying waves toward center. Otherwise, interfacial motion may become highly amplified at the center because of the high sensitivity of the amplitude to frequency and cell size.

Our theory is strictly valid for two-dimensional systems. Thus, the dynamics of three-dimensional interfacial waves such as in the rectangular liquid prism require numerical simulations for theoretical understanding, and more sophisticated methods to determine surface profiles experimentally. However, our analysis in the cylindrical coordinates can shed light on the essential characteristics of 3D interfacial waves which are excited at all the surrounding walls.
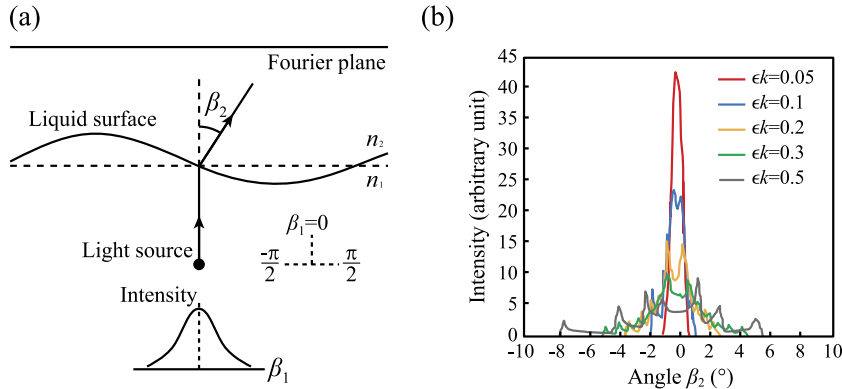
ACKNOWLEDGMENTS

FIG. 9. (a) Refraction of a light beam passing through a corrugated interface of different liquids with refractive indices n_1 and n_2. (b) The intensity of the beam arriving at the Fourier plane versus the angle β_2 for varying ϵk ($=2\pi\epsilon/\lambda$). The angular beam profiles are numerically calculated at the instance the displacement at $x = 0$ is zero while taking the damping coefficient $\alpha = 0.01\ \mu\mathrm{m}^{-1}$ and the width of liquid prism 0.2 mm.

APPENDIX: EFFECTS OF WAVE PROFILE OF LIQUID PRISM ON LIGHT BEAM

The beam profile as a result of refraction while propagating through a corrugated surface can be computed by Matlab based on Snell's law.[7,29] As shown in Fig. 9(a), the light beam from a line source, whose intensity is assumed to have the Gaussian profile with respect to the angle β_1, is refracted by an interfacial wave of a single mode: $\eta = \epsilon e^{-\alpha x}\cos(\omega t - kx)$. The intensity of the beam that arrives at the Fourier plane is plotted in Fig. 9(b) versus the angle β_2 for varying dimensionless wave amplitude, $\epsilon k = 2\pi\epsilon/\lambda$. We see that the shape of the beam profile is narrow resulting in a sharp image for small ϵk, while it broadens with growing ϵk leading to a blurred image. This plot allows us to predict the quality of optical images resulting from a corrugated liquid interface, which is an essential information in the design of the liquid prism.

[1] D. J. Acheson, *Elementary Fluid Dynamics* (Clarendon Press, Oxford, 1990).

[2] U. S. Jeng, L. Esibov, L. Crow, and A. Steyerl, "Viscosity effect on capillary waves at liquid interfaces," J. Phys.: Condens. Matter **10**, 4955-4962 (1998).

[3] J. C. Earnshaw and A. C. McLaughlin, "Waves at liquid surfaces: Coupled oscillators and mode mixing," Proc. R. Soc. A **433**, 663-678 (1991).

[4] A. D. Jenkins and S. J. Jacobs, "Wave damping by a thin layer of viscous fluid," Phys. Fluids **9**, 1256-1264 (1997).

[5] D.-G. Lee, J. Park, J. Bae, and H.-Y. Kim, "Dynamics of a microliquid prism actuated by electrowetting," Lab Chip **13**, 274-279 (2013).

[6] Y. Kwon, Y. Choi, K. Choi, Y. Kim, S. Choi, J. Lee, and J. Bae, "Development of micro variable optics array," in *Proceedings of IEEE Microelectromechanical Systems* (IEEE, 2014), pp. 72-75.

[7] Y. Kim, Y. Choi, K. Choi, Y. Kwon, and J. Bae, "Multi-view three-dimensional display system by using arrayed beam steering devices," SID Int. Symp. Dig. Tech. Pap. **45**, 907-910 (2014).

[8] Q.-L. Deng, C.-Y. Chen, S.-W. Cheng, W.-S. Sun, and B.-S. Lin, "Micro-prism type single-lens 3D aircraft telescope system," Opt. Commun. **285**, 5001-5007 (2012).

[9] P. F. McManamon, P. J. Bos, M. J. Escuti, J. Heikenfeld, S. Serati, H. Xie, and E. Watson, "A review of phased array steering for narrow-band electrooptical systems," Proc. IEEE **97**, 1078-1096 (2009).

[10] S. Terrab, A. M. Watson, C. Roath, J. T. Gopinath, and V. M. Bright, "Adaptive electrowetting lens-prism element," Opt. Express **23**, 25838-25845 (2015).

[11] J. Cheng and C. L. Chen, "Adaptive beam tracking and steering via electrowetting-controlled liquid prism," Appl. Phys. Lett. **99**, 191108 (2011).

[12] Y. Kim, Y. S. Choi, K. Choi, Y. Kwon, J. Bae, A. Morozov, and H. S. Lee, "Measurement of the optical characteristics of electrowetting prism array for three-dimensional display," Proc. SPIE **8643**, 864305 (2013).

[13] J. Bae, Y. S. Choi, K. Choi, Y. Kwon, H. Song, E. Kim, S. Choi, J. Lee, and S. Lee, "Arrayed beam steering device for advanced 3D displays," Proc. SPIE **8616**, 86160H (2013).

[14] H. Moon, S. K. Cho, R. L. Garrell, and C.-J. Kim, "Low voltage electrowetting-on-dielectric," J. Appl. Phys. **92**, 4080-4087 (2002).

[15] M. J. Sparnaay, "On the electrostatic contribution to the interfacial tension of semiconductor/gas and semiconductor/electrolyte interfaces," Surf. Sci. **1**, 213-224 (1964).

[16] K. Choi, Y. Kim, Y. Kwon, J. Bae, and Y. Choi, "3D image display apparatus including electrowetting lens array and 3D image pickup apparatus including electrowetting lens array," U.S. patent 9,354,439 (31 May 2016).

[17] S. Choi, "Robust electrowetting system for applications in display and parameter traking," Ph.D. thesis, Seoul National University, 2016.

[18] R. Malk, Y. Fouillet, and L. Davoust, "Rotating flow within a droplet actuated with AC EWOD," Sens. Actuators, B **154**, 191-198 (2011).

[19] M. K. Kilaru, J. Heikenfeld, G. Lin, and J. E. Mark, "Strong charge trapping and bistable electrowetting on nanocomposite fluoropolymer: $BaTiO_3$ dielectrics," Appl. Phys. Lett. **90**, 212906 (2007).

[20] T. B. Jones, J. D. Fowler, Y. S. Chang, and C.-J. Kim, "Frequency-based relationship of electrowetting and dielectrophoretic liquid microactuation," Langmuir **19**, 7646-7651 (2003).

[21] E. H. Lucassen-Reynders and J. Lucassen, "Properties of capillary waves," Adv. Colloid Interface Sci. **2**, 347-395 (1970).

[22] J. Zhang, D. Van Meter, L. Hou, N. Smith, J. Yang, A. Stalcup, R. Laughlin, and J. Heikenfeld, "Preparation and analysis of 1-chloronaphthalene for highly refractive electrowetting optics," Langmuir **25**, 10413-10416 (2009).

[23] L. D. Landau and E. M. Lifshitz, *Fluid Mechanics* (Elsevier, Oxford, 2004).

[24] H. Lamb, *Hydrodynamics* (Dover, New York, 1945).

[25] H.-Y. Kim, "On thermocapillary propulsion of microliquid slug," Nanoscale Microscale Thermophys. Eng. **11**, 351-362 (2007).

[26] V. G. Levich and S. Technica, *Physicochemical Hydrodynamics* (Prentice-Hall, Englewood Cliffs, NJ, 1962).

[27] A. Ghosh and P. Fischer, "Chiral molecules split light: Reflection and refraction in a chiral liquid," Phys. Rev. Lett. **97**, 173002 (2006).

[28] X. Mao, S. C. S. Lin, M. I. Lapsley, J. Shi, B. K. Juluri, and T. J. Huang, "Tunable Liquid Gradient Refractive Index (L-GRIN) lens with two degrees of freedom," Lab Chip **9**, 2050-2058 (2009).

[29] E. Hecht, *Optics* (Addison-Wesley, Reading, 1979).